RESEARCH ARTICLE | JUNE 07 2022

A computational fluid dynamics study on rimming flow in a rotating cylinder

H. Sadeghi ; L. Diosady; B. Blais

Physics of Fluids 34, 063304 (2022)
https://doi.org/10.1063/5.0093351

Physics of Fluids ARTICLE scitation.org/journal/phf

A computational fluid dynamics study on rimming flow in a rotating cylinder

Cite as: Phys. Fluids **34**, 063304 (2022); doi: 10.1063/5.0093351
Submitted: 28 March 2022 · Accepted: 18 May 2022 ·
Published Online: 7 June 2022

H. Sadeghi,[1,2,a)] L. Diosady,[2] and B. Blais[1]

AFFILIATIONS

[1]Research Unit for Industrial Flows Processes (URPEI), Department of Chemical Engineering, École Polytechique de Montréal, P.O. Box 6079, Stn Centre-Ville, Montréal, Quebec H3C 3A7, Canada
[2]Pratt and Whitney Canada, 1801 Courtneypark Drive, Mississauga, Ontario L5T 1J3, Canada

[a)]Author to whom correspondence should be addressed: hamed.sadeghi82@gmail.com

ABSTRACT

Extensive computational fluid dynamics (CFD) simulations were conducted to study "rimming" flow in a partially filled horizontally rotating cylinder. These flows are encountered in aero-engine bearing chambers, which often exhibit complex two-phase flow scenarios as well as in multiple other engineering applications. In this study, a robust numerical scheme to model two-phase rimming flow has been adopted and validated against analytical expression and experimental data obtained from the literature. Additionally, a vast parametric study of the flow conditions has been performed. We used the volume of fluid method to solve the system of multi-phase flow governing equations and track the interface of rimming flow. The time-dependent gas–liquid interface was resolved, and the liquid-film thickness was determined. First, we performed our simulations within small to moderate ranges of Reynolds and Bond numbers and compared our results with previously reported analytical and experimental investigations. The present CFD results were found to be in very good agreement with previously reported data, both in identifying different regimes reported in the literature for rimming flow and in liquid-film thickness predictions. We also performed several additional simulations at much larger and practical ranges of Reynolds and Bond numbers, beyond the limitations imposed in previous analytical and experimental investigations on thin-film flows. We showed that three different flow regimes—shear-dominated, transitional, and gravitational-dominated—are attainable for the rimming flow for different combinations of Reynolds, Bond, and gravitational numbers. The present numerical results led us to propose a new map of rimming flow regimes by introducing functions of the Froude number and capillary number, which successfully identify and separate these regimes for a significant number of flow conditions.

I. INTRODUCTION

In many industrial applications, thin-film flows play an important role, for example, cooling and lubricating transmission systems. A thin-film flow is mainly represented by a layer of liquid formed near a solid wall, which is separated from the gas flow. The prediction of a thin-film flow is of keen interest for many industrial systems, including gas–liquid separators, capillary-driven and rotating heat pipes, devices containing surface cooling/heating, and aero-engine bearing chambers (O'Brian and Schwartz, 2002; Mecke and Rauscher, 2005; Singh *et al.*, 2004; Willems *et al.*, 2010; and Kay *et al.*, 2014).

Of particular interest to the present work is the coating of liquid flow in the form of a thin film on the interior of a constantly rotating horizontal cylinder, which is typically called the rimming flow (Ruschak and Scriven, 1976 and Moffatt, 1977). In aero-engine bearing chambers, rimming flow is a consequence of the interaction of forces due to shear stress, gravitational field, surface tension, and the inertial force, which lead to different forms and shapes of liquid films.

The basis for many previous findings to investigate thin-film flow, in particular analytical and numerical solutions, has been the "two-dimensional (2D)" form of classical rimming flow, as shown in Fig. 1. This has been also a benchmark problem for an idealized model of an aero-engine bearing chamber, albeit restricted only to low and medium ranges of Reynolds numbers. The objective of the present study is to apply available computational methods for the simulation of 2D rimming flow in a partially filled horizontally rotating cylinder.

Rimming flow in a partially filled horizontally rotating cylinder has been extensively studied by many researchers experimentally, analytically, and numerically (Ruschak and Scriven, 1976; Moffatt, 1977; Thoroddsen and Mahadevan, 1997; O'Brian and Gath, 1988; Johnson, 1988; Tirumkudulu and Acrivos, 2001; Ashmore *et al.*, 2003; Evans *et al.*, 2005; Chen *et al.*, 2007; Benilov *et al.*, 2008; Kay *et al.*, 2013, 2014; Singaram *et al.*, 2014; Kakimpa *et al.*, 2016; Kumawat and Tiwari, 2017b, 2017a, 2018; Nicholson *et al.*, 2019; and Mitchell *et al.*, 2022). Among these works, several authors have studied the behavior

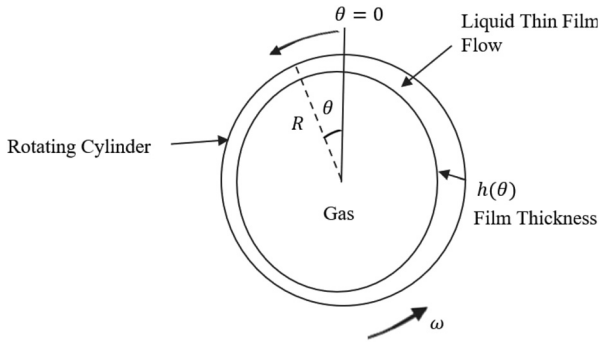

FIG. 1. Thin film rimming flow inside a rotational cylinder and coordinate used.

of a thin-film rimming flow through a combination of analytical and numerical approaches known as depth-averaged numerical approximations (Ashmore *et al.*, 2003; Benilov *et al.*, 2008; Kay *et al.*, 2014; and Kakimpa *et al.*, 2016). For example, Kakimpa *et al.* (2016) referred to these methods as the Eulerian thin-film models (ETFMs) in which generally the three-dimensional (3D) Navier–Stokes equations are reduced to a set of 2D thin-film equations since they are depth-averaged across the film thickness. In particular, the study performed by Ashmore *et al.* (2003) highlights important features of 2D thin-film rimming flow and is of particular attention to the present paper. They discussed that based on the choice of parameters such as the diameter of the cylinder, the liquid properties, filling fraction, and the rotational speed, which can correspond to the ratio of gravitational to viscous forces, three different kinds of flow regimes are attainable for 2D rimming flow, which are *shear-dominated (smooth) flow*, *transitional (shock) flow*, and *gravitational dominated (pool) flow*, as illustrated in Fig. 2.

The shear-dominated regime is formed when the viscous forces overcome the gravitational forces. On the other hand, in the pool regime, gravitational forces are dominant. The shock flow condition lies between smooth and pool flow conditions. A detailed description of different flow transitions for rimming flow in a partially filled horizontal rotating cylinder can be found in the studies by Ashmore *et al.* (2003) and Kakimpa *et al.* (2016). Ashmore *et al.* (2003) measured the ratio of the gravitational to the viscous forces by the dimensionless parameter, defined as the gravitational number,

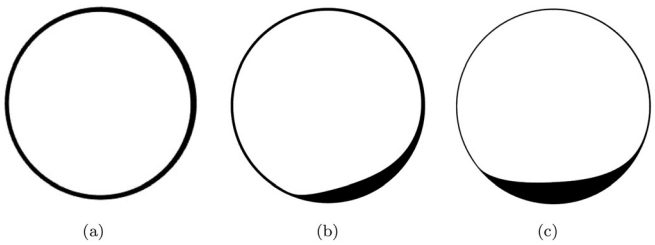

FIG. 2. Thin film rimming flow regimes: (a) shear-dominated (smooth) flow, (b) a transitional (shock) flow, and (c) a gravitational-dominated (pool) flow inspired by (Ashmore *et al.*, 2003 and Kakimpa *et al.*, 2016).

$$\lambda = \frac{A^2 \rho g R}{\mu \omega}, \tag{1}$$

where A is the filling fraction of fluid inside the cylinder, ρ is the density, g is the gravitational constant, R is the radius of the cylinder, μ is the dynamic viscosity, and ω is the rotation rate (rad/s). It should be noted that this dimensionless number (as well as other upcoming dimensionless numbers) is constructed only based on liquid properties. The solutions for three different regimes of the rimming flow have been reported to exist in the ranges of λ as follows: the shear-dominated regime for $0 < \lambda \lesssim 2$; the transitional regime for $2 \lesssim \lambda \lesssim 5$; and the gravitational-dominated regime for $\lambda \gtrsim 5$ (Ashmore *et al.*, 2003). According to previous analytical and numerical work on the literature (Tirumkudulu and Acrivos, 2001; Ashmore *et al.*, 2003; Kay *et al.*, 2013; and Kakimpa *et al.*, 2016), there are also other restrictions to identify each of these regimes. They can be recognized through two other dimensionless parameters, which are the Bond number defined as

$$Bo = \frac{\rho g R^2}{A\sigma}, \tag{2}$$

where σ represents surface tension, and the Reynolds number is defined as

$$Re = \frac{\rho \omega R^2}{\mu}. \tag{3}$$

In many lubrication analyses (e.g., Ashmore *et al.*, 2003 and Kay *et al.*, 2013), the shear-dominated, transitional, and pool regimes can be only identified analytically at small Re, in the sense that $A^2 Re \ll 1$, while $A \ll 1$. Perhaps the major observed numerical and analytical challenge has been the unstable shock and pool solutions, which have been mainly noted when surface tension effects are small or completely neglected ($Bo \to \infty$) (Ashmore *et al.*, 2003; Benilov *et al.*, 2008; and Kakimpa *et al.*, 2016). This has led to more rigorous analytical studies in which surface tension effects were included (in which Bo is finite) and ended up with more stable smooth, shock, and pool solutions (Ashmore *et al.*, 2003 and Benilov *et al.*, 2008). For example, Ashmore *et al.* (2003) used analytical and numerical methods, while including surface tension that was identified through the Bond number and studied the steady solutions in all low, medium, and large values of λ. The Bond number in their work varied between 10–1000, and the limitation on the Reynolds number was $A^2 Re \ll 1$, while $A \lesssim 0.3$. Some other analytical and numerical studies (Kay *et al.*, 2014 and Kakimpa *et al.*, 2016) also showed that stable shock and pool solutions were only attainable if a surface tension at around the first-order of approximation is applied. Therefore, stable solutions could only be achieved when using a surface tension coefficient on two orders of magnitude higher than that observed in practical applications (Kakimpa *et al.*, 2016).

Thus, despite the significant studies that have been conducted in the context of 2D rimming flow so far, there are still a number of questions that need to be addressed. First, the solutions have been found to be very dependent on surface tension (or Bond number), and the solutions were only stable when a high surface tension was used. In practical application, very high surface tension may not be realistic. Thus, we try to provide a better understanding of the dependency of solutions on surface tension (Bond number) in real applications. The

second question will be whether the identified rimming flow regimes in low and medium Re numbers can be also observed at large Re numbers, where most real applications operate. The other important question to be addressed is whether the solutions, which have been analytically described, can be also observed experimentally or computationally. This is again mainly because there are restrictions that have been placed on different parameters when the problem was studied analytically that can be reduced through experimental or computational fluid dynamics (CFD) work.

Experimental studies for realistic geometries and operating conditions, which may produce more accurate models, are expensive and time consuming. A validated computational fluid dynamics (CFD) analysis of such cases emerges as an attractive alternative, particularly for parametric studies of different effects. CFD results may eventually better complement analytical ones for the purposes of understanding different rimming flow regimes. A literature survey, however, revealed no significant computational research on these topics.

The objective of this work is to apply a robust multi-phase computational fluid dynamics method to simulate shear-dominated (smooth), transitional (shock), and gravitational-dominated (pool) flows of 2D rimming flow in a partially filled horizontally rotating cylinder. We particularly focus on open questions in this topic, which include studying the impact of flow parameters such as the Bond number on identifying different regimes, providing new solutions beyond the analytical and experimental restrictions, and identifying flow regimes at large Reynolds numbers. First, we validate the chosen method against reliable experimental and analytical data at low and moderate Reynolds and Bond numbers. Having validated the CFD method, we apply it to a few representative cases in larger ranges of Reynolds and Bond numbers. Finally, we introduce a new map of rimming flow regimes for all investigated flow conditions through a combination of dimensionless numbers, namely the filling fraction, Froude, and capillary numbers. To the best of our knowledge, this is the first study of 2D rimming flow in a partially filled horizontally rotating cylinder using a CFD approach.

II. COMPUTATIONAL DETAILS

A. Computational geometry, boundary, and initial conditions

The computational geometry for this research is illustrated in Fig. 1, which allows us to study the thin film behavior inside a partially filled, horizontal rotating cylinder. Here, a 2D polar coordinate system (r, θ) is applied, where the origin is placed at the center of the cylinder. Thin-film thickness measurements are conducted in the azimuthal direction, in which θ is varied from 0 to 2π, in the sense of rotation with $\theta = 0^\circ$ coinciding with the upward vertical. Here, h_θ is the interface height or liquid film thickness, and the radius of the cylinder is denoted by R. The cylinder is rotating in the counter clock-wise direction with rotational speed ω, which is realized through a rotating wall boundary condition in our simulations. At the start of the simulations ($t = 0$), the system was filled with a pool of liquid, which was patched at the bottom of the cylinder. Additionally, a very thin liquid film layer of around $0.02R$ thickness was patched on the wall. It was found that patching of the thin film layer helps to reach the steady-state solution faster and additionally overcomes numerical de-wetting of the walls. The filling faction A was identified through the fraction of liquid that initially filled the cylinder. The rest of the cylinder was filled with a gas at rest (see Fig. 3).

B. Computational method

All simulations were performed using the computational fluid dynamics (CFD) package ANSYS fluent using very recent versions (2020R2 and 2021R2). The computational method consists of solving a system of two-dimensional, time dependent equations. In order to resolve the interface between gas and liquid in the cylinder, we used the volume of fluid (VOF) method (Hirt and Nichols, 1981). This method models the flow of two immiscible fluids by solving a single set of continuity and momentum equations for a continuous fluid in the following form:

$$\frac{\partial \bar{\rho}}{\partial t} + \vec{\nabla} \cdot \left(\bar{\rho}\vec{V}\right) = 0, \tag{4}$$

$$\frac{\partial}{\partial t}\left(\bar{\rho}\vec{V}\right) + \vec{\nabla} \cdot \left(\bar{\rho}\vec{V} \otimes \vec{V}\right) = -\vec{\nabla}p + \bar{\rho}\vec{g} + \vec{\nabla} \cdot \bar{\bar{\tau}} + \vec{F}_{ST}. \tag{5}$$

Here, $\bar{\bar{\tau}}$ is the stress tensor: $\bar{\bar{\tau}} = \bar{\mu}(\vec{\nabla}\vec{V} + \vec{\nabla}\vec{V}^T)$, where the superscript T denotes the transpose. The local "average" fluid density $\bar{\rho}$ and viscosity $\bar{\mu}$ were from the volume fractions α_l of the liquid and α_g of the gas within each computational cell and the densities ρ_l of the liquid and ρ_g of the gas as $\bar{\rho} = \alpha_l\rho_l + \alpha_g\rho_g$ and $\bar{\mu} = \alpha_l\mu_l + \alpha_g\mu_g$. It should be noted that the volume fractions α_l of the liquid and α_g obey the constraint $\alpha_l = 1 - \alpha_g$.

Additionally, $\vec{F}_{ST}$ is the surface tension force approximated using a continuum surface force (CFS) model (Brackbill *et al.*, 1992) as follows: $\vec{F}_{ST} = \sigma\kappa\vec{\nabla}\alpha_g$, where σ is the surface tension of the gas–liquid mixture and κ is the local interface curvature.

The tracking of the interface between the phases is accomplished by the solution of a continuity equation for the volume fraction α_g of gas in the following form:

$$\frac{\partial \alpha_g}{\partial t} + \vec{\nabla}.\left(\alpha_g\vec{V}\right) = 0. \tag{6}$$

It is apparent that the governing equations are coupled through the velocity $\vec{V}$.

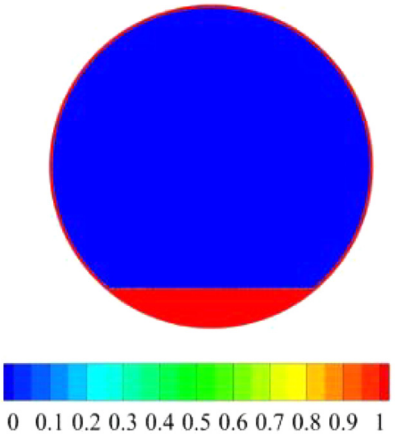

FIG. 3. Gas (blue) and liquid (red) distribution at the initial time in the cylinder shown through a volume fraction contour.

Time discretization was carried out using an implicit second-order Euler scheme. To discretize the interface advection, we used a compressive scheme, which has been recently implemented in Ansys Fluent (ANSYS, 2020). We also used an upwind-based scheme, known as a physical influence scheme, to treat the convection terms of the momentum and other transport equations at the cell faces. In this work, we benefit from the SIMPLE algorithm to couple the pressure and velocity fields and a standard two-equations SST $k-\omega$ turbulence model to model turbulence (Menter *et al.*, 2003). For low *Re*, the flow remained mainly laminar; thus, the choice of turbulence or laminar models did not affect the flow pattern and film thickness. At high *Re*, using other turbulence models, such as $k-\omega$ and $k-\epsilon$, had no significant effect on the present findings.

C. Ranges of simulations

Numerical simulations have been carried out for different combinations of Reynolds numbers (*Re*), Bond numbers (*Bo*), and gravitational numbers (λ), in the ranges that are displayed in Fig. 4. These ranges of simulations allowed us, first, to validate and verify our simulations with the previously reported experimental and analytical data, which were performed at lower ranges of *Re* and *Bo*. Then, once an adequate validation of the present models has been achieved, we performed the simulations at larger Re and Bo, to get closer to the real application situations.

D. Steady-state solutions

As representative results of solution convergence, Fig. 5(a) shows the temporal evolution of the liquid film thickness at $\theta = 0°$ and $\theta = 180°$, which, respectively, coincide with the downward and upward vertical positions on the cylinder, for $Re = 300$, $Bo = 100$, and $\lambda = 2$. Since the system was initially patched with liquid, the film thickness began to temporally evolve from some adjusted initial non-zero values. It can be seen that the solutions eventually achieved steady states within relatively short physical times, here about 1 s. As another measure of the accuracy of the present numerical studies, we also checked the balance of filling fraction and mass in the system as shown in Fig. 5(b), which indicates a perfect balance in mass and filling fraction in the cylinder. It should be noted that for cases with larger values of *Re* and *Bo*, more disturbances were observed in the thin-film thickness measurements and the flow was more in a transient state. For these conditions, a statistically steady-state solution was calculated. Here, the average film thickness was checked to ensure a statistically steady-state is achieved. For example, it was found that, for the case with $Re = 4.3 \times 10^4$, $Bo = 2.2 \times 10^5$, and $\lambda = 5$, after 1 s from the start, the average liquid film thickness over the first 0.5 s was within 2%–3% of the corresponding averages over the next 0.5 s (Fig. 6).

E. Mesh independence studies

A butterfly grid, which is composed of a Cartesian mesh in the center of the cylinder combined with a structured mesh around, was fitted to the computational domain (see, e.g., Fig. 7). The mesh was generated with a growth rate of 1.2 to ensure a smooth transition between the fine mesh near the wall to the cell in the middle. This grid was deemed to be well suited to the circular geometry in the context of two-phase flow (Hernandez-Perez *et al.*, 2011).

We have studied the thin-film flow using different mesh sizes to measure the sensitivity of our numerical solutions to the mesh size. Representative results are shown in Table I for a low Reynolds and Bond numbers case and in Table II for a large Reynolds and Bond numbers case. In these tables, we show the percent changes of predicted properties as a progressively finer mesh was used. The parameter chosen for the mesh dependence study is the normalized liquid film-thickness, which will be frequently used throughout this study, defined as (Ashmore *et al.*, 2003)

$$\tilde{h}_\theta = \frac{h_\theta}{RA}. \tag{7}$$

Here, the percent change is calculated as the difference of this quantity for finer and coarser mesh divided by the computed value of the coarser mesh at some selected locations. Based on these analyses, and

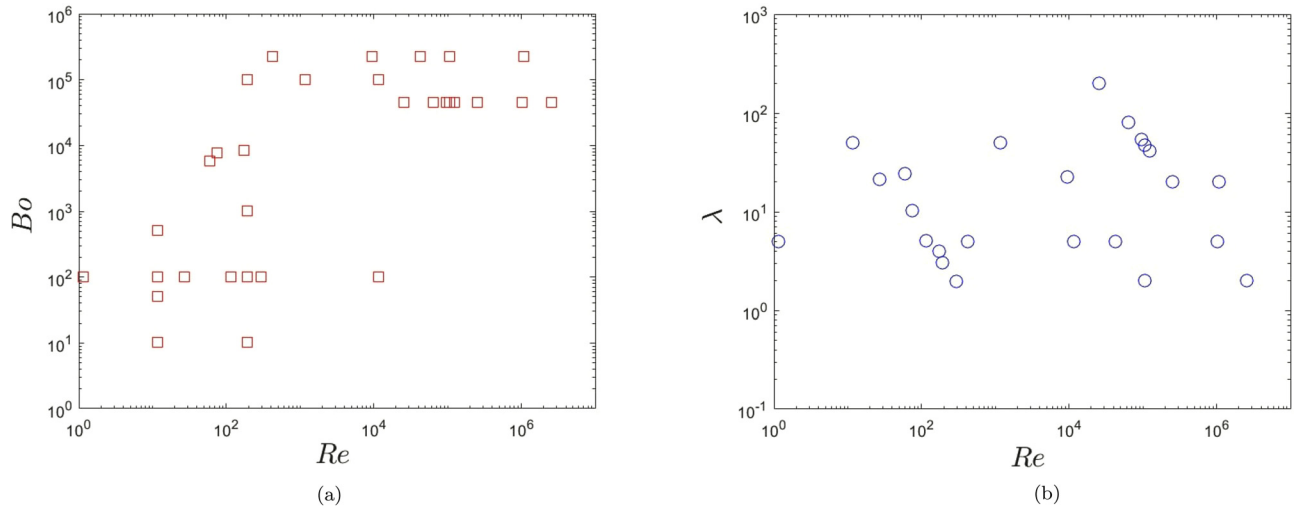

(a) (b)

FIG. 4. Range of dimensionless numbers for the simulations in the present study: (a) Bond number vs Reynolds number and (b) gravitational number vs Reynolds number.

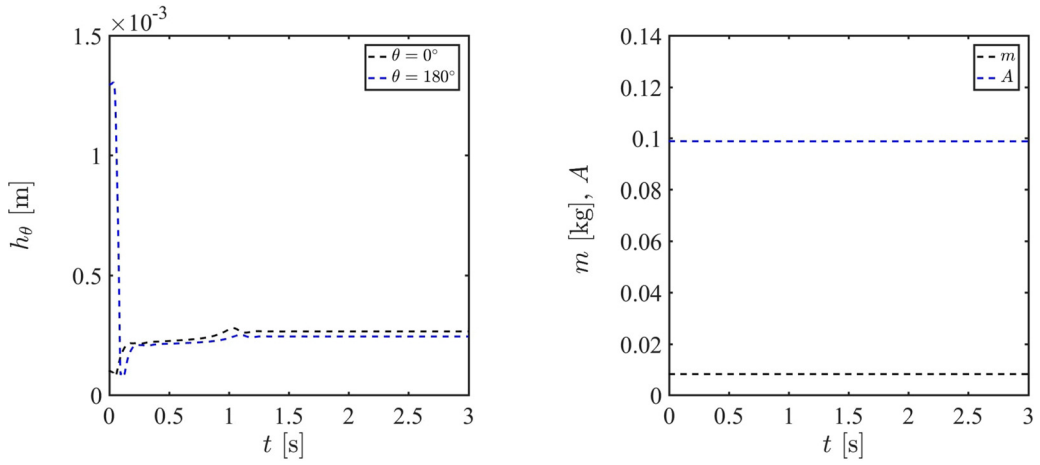

FIG. 5. Temporal evolution of (a) liquid film thickness at $\theta = 0^\circ$ and $\theta = 180^\circ$ and (b) filling fraction A and mass m in the cylinder for $Re = 300$, $Bo = 100$, $\lambda = 2$, and $A = 0.1$.

to keep the computational cost reasonable, we chose a mesh composed of 800 000 cells for the majority of simulations. We also reported the normalized first cell size ($\tilde{\Delta}y_1 \equiv \Delta y_1/RA$) and cell length interval ($\tilde{\Delta}x \equiv \Delta x/R$) in Tables I and II.

F. Time-step dependence studies

In this study, we assessed the importance of selecting an appropriate time step to reach a smoothly converging solution. Thus, we chose a range of time-steps from $\Delta t = 10^{-5}$–10^{-3} s that kept the Courant–Friedrichs–Lewy (CFL) number in a range from 0.1–10. Our simulations showed that the choice of the time step was very crucial to achieve a converged solution since a time step larger than $\Delta t = 10^{-3}$ s, which corresponded to CFL > 1, led to both diverged and incorrect flow solutions. As an example, Fig. 8 shows the temporal evolution of the film thickness at $\theta = 180^\circ$ and the mass conserved in the system for three choices of time-steps of $\Delta t = 10^{-5}, 10^{-4}$, and 10^{-3} s, which, respectively, correspond to maximum Courant–Friedrichs–Lewy numbers of CFL = 0.1, 1, and 10. It should be noted that the grid size and flow conditions were identical in all cases. As can be seen, both $\Delta t = 10^{-5}$ and 10^{-4} s provided almost the identical state-sate solutions with the mass in the cylinder fully conserved; however, for the case with $\Delta t = 10^{-3}$ s, the mass (and as well the film-thickness) was lost in the system. Thus, in this study, we mostly selected $\Delta t = 10^{-5}$ s, which ensured that the CFL remained less than 1.

III. COMPUTATIONAL FLUID DYNAMICS (CFD) RESULTS

CFD simulations have been performed to study the rimming flow in a rotating, partially filled, horizontal cylinder for different and

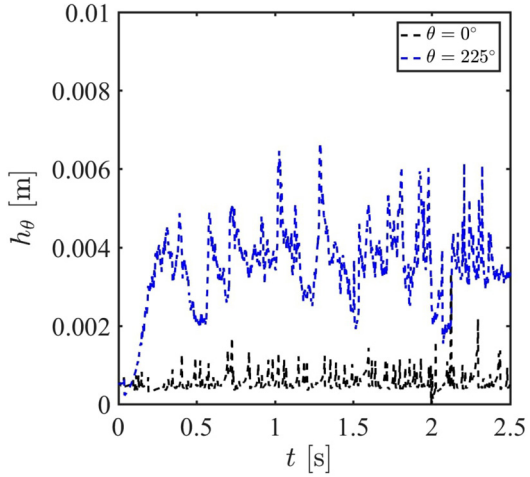

FIG. 6. Temporal evolution of liquid film thickness at $\theta = 0^\circ$ and $\theta = 225^\circ$ for $Re = 4.3 \times 10^4$, $Bo = 2.2 \times 10^5$, and $\lambda = 5$.

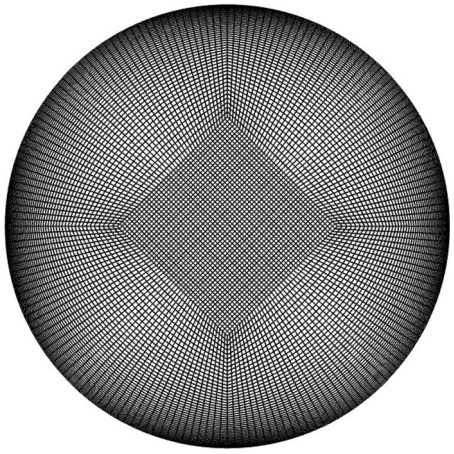

FIG. 7. An example of the butterfly grid with around 28 000 cells used to mesh the cylinder.

TABLE I. Mesh dependence study for a 2D rimming flow with $Re = 121$, $Bo = 100$, $\lambda = 5$, and $A = 0.1$ at $\theta = 0°$. The flow was in a transitional regime.

Number of cells	$\tilde{\Delta}y_1$	$\tilde{\Delta}x$	$\tilde{h}_\theta$	Percent change
28 000	0.283	0.0566	0.2958	0.7
200 000	0.014	0.0213	0.2937	0.1
400 000	0.0088	0.0156	0.2934	0.1
800 000	0.0065	0.0056	0.2931	0.1
1 200 000	0.0048	0.0021	0.2928	⋯

TABLE II. Mesh dependence study for a 2D rimming flow with $Re = 4.27 \times 10^4$, $Bo = 2.2 \times 10^5$, $\lambda = 5$, and $A = 0.02$ at $\theta = 225°$.The flow was in a transitional regime.

Number of cells	$\tilde{\Delta}y_1$	$\tilde{\Delta}x$	$\tilde{h}_\theta$	Percent change
28 000	1.415	0.0565	0.5021	79
200 000	0.07	0.0213	0.9031	68
400 000	0.044	0.0156	1.5225	0.8
800 000	0.0325	0.0056	1.5355	0.3
1 200 000	0.024	0.0021	1.5405	⋯

extensive combinations of Re, Bo, and λ. The particular interest was to validate the CFD models and identify flow regimes, beyond what has been observed in previous analytical and experimental investigations. As such, we present the results based on the Reynolds numbers as follows: low-to-medium Reynolds numbers for $Re \lesssim 1000$ and large Reynolds numbers for $Re > 1000$. We separately investigate the effect of Bo and λ in $Re \lesssim 1000$ and $Re > 1000$. Based on the current CFD and previous experimental/analytical results, a flow transition map will be presented in this article. Note that, unless otherwise stated, the

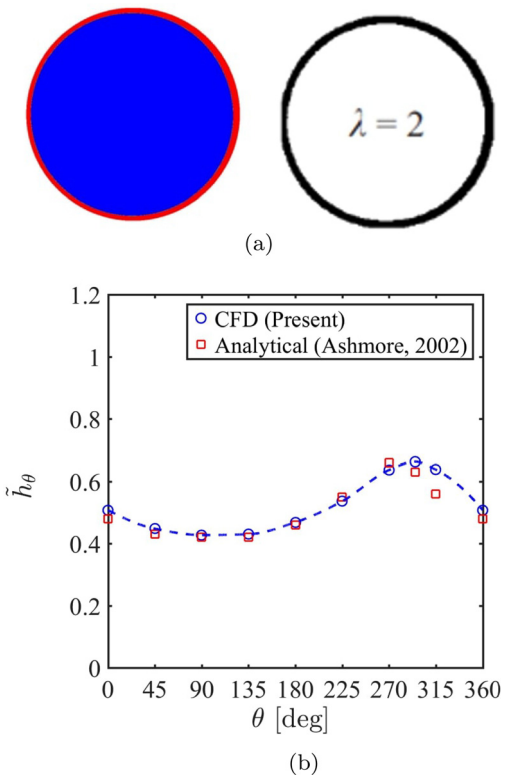

FIG. 9. (a) Contour plot of the volume fraction of liquid from the present CFD with liquid identified by color red (left) and plot of numerical solution from Ashmore *et al.* (2003) with liquid identified by color black (right); and (b) calculated film-thickness ($\tilde{h}_\theta$) from the present CFD together with equivalent predictions from Ashmore *et al.* (2003) during steady-state. In all cases, $A = 0.1$, $\lambda = 2$, $Re = 300$, and $Bo = 100$.

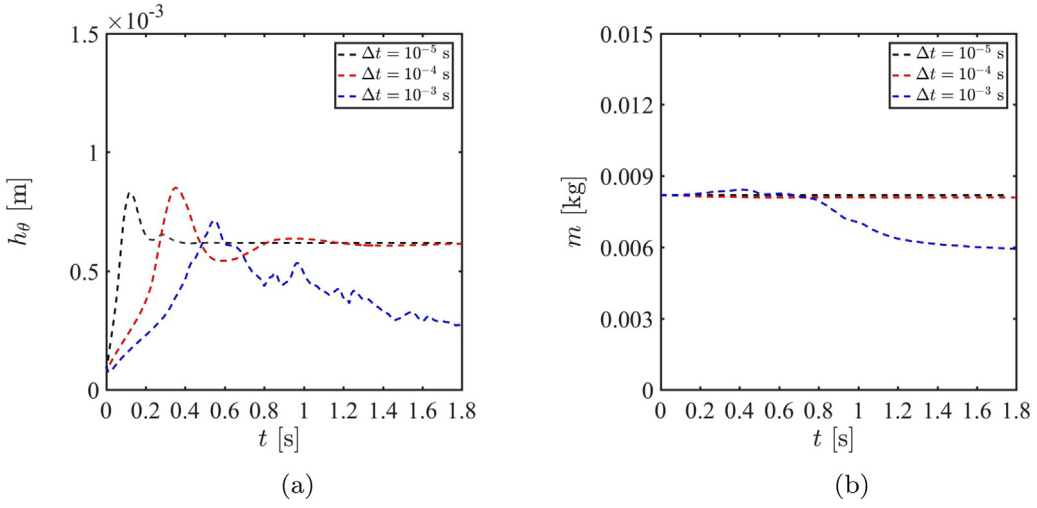

FIG. 8. Temporal evolution of (a) liquid film thickness at $\theta = 0°$ and $\theta = 180°$ and (b) mass, m, in the cylinder for different time-steps of $\Delta t = 10^{-5}$, 10^{-4}, and 10^{-3} s for $Re = 121$, $Bo = 100$, $\lambda = 5$, and $A = 0.1$. The grid size was 800 000 cells.

presented results correspond to simulations for air–oil mixtures at a practical operating pressure, as noted in Sec. II C.

A. CFD results: $Re \lesssim 1000$

1. Validation and verification

In this section, we presented the numerical results for $Re \lesssim 1000$ and validated them against analytical and experimental data that have been reported for a rotating, partially filled, horizontal cylinder. First, we compared our results with the analytical solutions of Ashmore *et al.* (2003), who showed that for $A^2Re < 1$ and within a small finite range of Bond number, the gravitational number λ can identify all three rimming flow regimes as follows: the shear-dominated regime for $0 < \lambda \lesssim 2$, the transitional regime for $2 \lesssim \lambda \lesssim 5$, and the gravitational-dominated regime for $\lambda \gtrsim 5$. To compare our CFD results with the analytical solutions of Ashmore *et al.* (2003), we conducted simulations under the same conditions (as noted in their Fig. 2) with $A = 0.1$, $Bo = 100$, and $\lambda = 2, 5$, and 20, which correspond to $Re = 300$, 120, and 30, respectively. Figures 9–11 show representative contours of the volume fraction of liquid and normalized liquid film-thickness ($\tilde{h}_\theta$) during the steady-state for $\lambda = 2, 5$, and 20. The corresponding analytical solutions are also included in these figures. Results show very good agreement between the thin-film

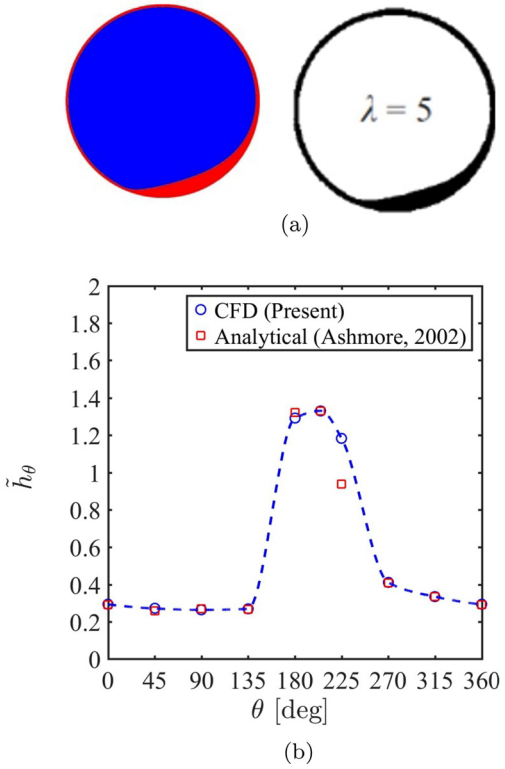

FIG. 10. (a) Contour plot of the volume fraction of liquid from the present CFD with liquid identified by color red (left) and plot of numerical solution from Ashmore *et al.* (2003) with liquid identified by color black (right); (b) calculated film-thickness ($\tilde{h}_\theta$) from the present CFD together with equivalent predictions from Ashmore *et al.* (2003) during steady-state. In all cases, $A = 0.1$, $\lambda = 5$, $Re = 120$, and $Bo = 100$.

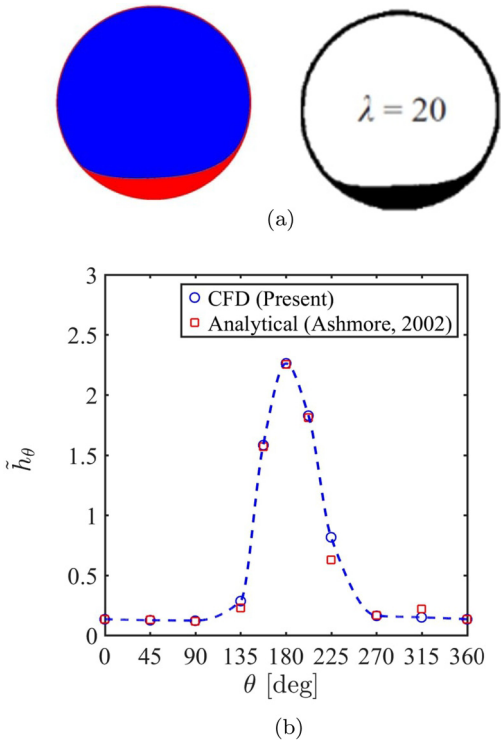

FIG. 11. (a) Contour plot of the volume fraction of liquid from the present CFD with liquid identified by color red (left) and plot of numerical solution from Ashmore *et al.* (2003) with liquid identified by color black (right); (b) calculated film-thickness ($\tilde{h}_\theta$) from the present CFD together with equivalent predictions from Ashmore *et al.* (2003) during steady-state. In all cases, $A = 0.1$, $\lambda = 20$, $Re = 30$, and $Bo = 100$.

solutions of Ashmore *et al.* (2003) and the present CFD simulations. As can be seen from Fig. 9, at the lowest λ, a near-uniform shear-dominated flow was achieved, in which $\tilde{h}_\theta$ oscillates close to half. A transient regime was also satisfactorily achieved for the case with $\lambda = 5$ as shown in Fig. 10. Here, the stable solutions were obtained by the use of the current CFD model, while a standard surface tension in an aero-engine bearing chamber (i.e., $\sigma = 0.0245$ N m^{-1}) was used. This finding is contrary to the results of the ETFM model adopted by Kakimpa *et al.* (2016) who found large values of surface tension are required to obtain stable solutions for the transitional regime. At the largest gravitational number ($\lambda = 20$), which corresponds to a very low rotational speed, most of the liquid was at the bottom with a thin film arising out of the pool wetting the entire inner surface of the cylinder Fig. 11.

The results from the present simulations for different combinations of *Re*, *Bo*, and λ are plotted together with corresponding experimental measurements of Tirumkudulu and Acrivos (2001) in Fig. 12. These results also show good agreement between the present CFD simulations and the experimental measurements.

2. Effects of the Bond number

Having predicted successfully three different regimes of steady solutions for a rimming flow, we examined the effects of the Bond number on the flow behavior for Re $\lesssim$1000. As noted in the study by

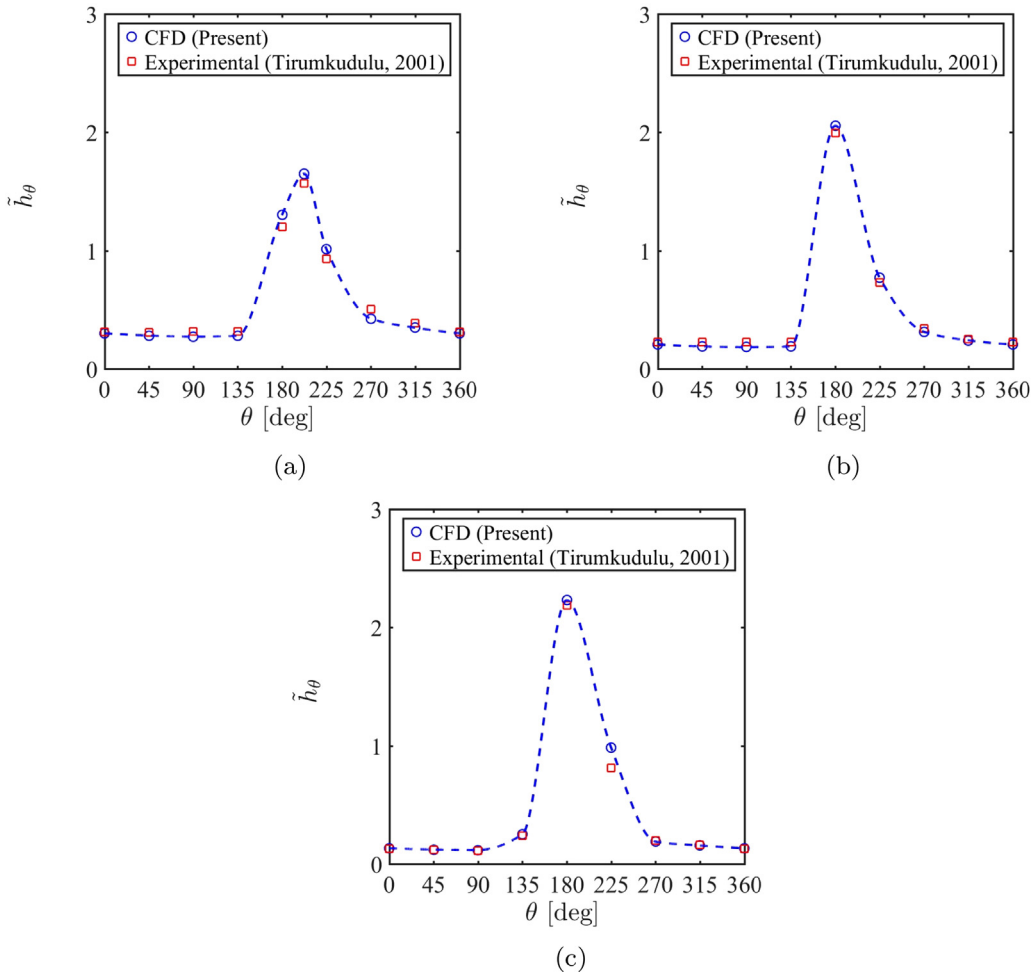

FIG. 12. Calculated $\tilde{h}_\theta$ from the present CFD together with experimental measurements from Tirumkudulu and Acrivos (2001) under the following conditions: (a) $\lambda = 4$, $A = 0.1261$, $Bo = 8280$, and $Re = 173$; (b) $\lambda = 10$, $A = 0.1198$, $Bo = 7783$, and $Re = 75$; and (c) $\lambda = 24$, $A = 0.1625$, $Bo = 5730$, and $Re = 59$.

Ashmore *et al.* (2003), three different regimes of steady solutions can be identified in the limits in which the ratio of gravitational to viscous forces is small, moderate, or large, within a finite limit of Bond number (e.g., $Bo = 100$). Here, with the use of the CFD, we study the effects of Bond number through Figs. 13–15 for $\lambda = 2, 3$, and 5, respectively. To compare with Ashmore *et al.* (2003), we also provided the analytical solution for $Bo = 100$. Figure 13(a) shows contour plots of the volume fraction of liquid, whereas Fig. 13(b) shows simulated $\tilde{h}_\theta$, for $A = 0.1$, $\lambda = 2$. Here, the Bond number was varied between 10–100 000. It was found that the rimming flow was insensitive to Bo and remained shear-dominated, unless at a very large Bond number of $Bo = 10\,000$. For this large Bo case, a transitional regime appeared. Under this condition, the flow is becoming transient (vs mostly fully steady-state) and we see pockets of air within the liquid. Further increasing Bo ($Bo = 100\,000$), a pool regime is identified, while we can see more liquid droplets within the air.

Figure 18 shows plots of the numerical simulations of the similar quantities for $A = 0.1$ and $\lambda = 3$, while Bo was varied between 10–100 000. It can be observed that there is an increase in the pool of liquid at the bottom of the cylinder with increasing Bo. For $Bo = 10$, the flow was mainly distributed around the entire inner surface of the cylinder. A transitional flow regime can be observed for $Bo = 100$ and 1000. For $Bo = 10\,000$, the flow was still in the transitional regime while pockets of air appeared within the liquid first at this Bo. It can be seen that the region where the fluid accumulated the most is around $\theta = 225°$. At the front of this region, the gradient of the interface is larger for $Bo = 10\,000$, and the solution exhibits a strong asymmetry about $\theta = 180°$. However, for $Bo = 100\,000$, a more pool flow can be identified with the largest thickness of liquid spotted at $\theta = 180°$. Figure 15 shows plots of the numerical simulations for $A = 0.1$, $\lambda = 50$, while Bo was varied between 10–500. Here, it was found that a pool flow regime was maintained for all Bond numbers with the largest film thickness observed at $\theta = 180°$. With increasing Bo, the amount of oil pooling at the bottom of the cylinder increases, while the film thins on the remainder of the cylinder. At low Re, with large λ, a steady-state solution was obtained for all Bo considered.

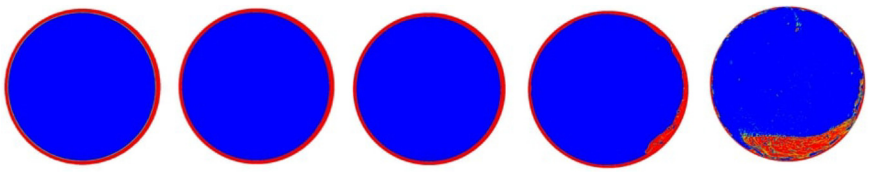

(a)

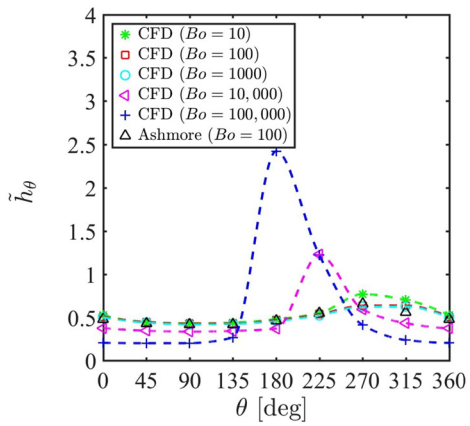

(b)

FIG. 13. (a) Contour plots of the volume fraction of liquid. From left to right: $Bo = 10$; $Bo = 100$; $Bo = 1000$; $Bo = 10\,000$; and $Bo = 100\,000$. (b) Calculated $\tilde{h}_\theta$ from the present CFD for $Bo = 10$–$100\,000$ together the solution from Ashmore *et al.* (2003) for $Bo = 100$. In all cases, $A = 0.1$, $\lambda = 2$, and $Re = 300$.

B. CFD results: Re > 1000

After validation of the present simulations with the analytical and experimental data in the literature for lower *Re*, we performed additional simulations of the rimming flow for a larger range of Reynolds numbers, namely, $Re > 1000$. The majority of the previously discussed simulations considered air–oil mixtures at the relatively low ranges of *Re* and *Bo*, which allowed us to match with the analytical and experimental studies in the literature. However, most industrial

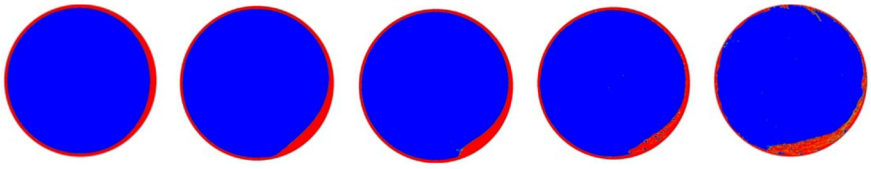

(a)

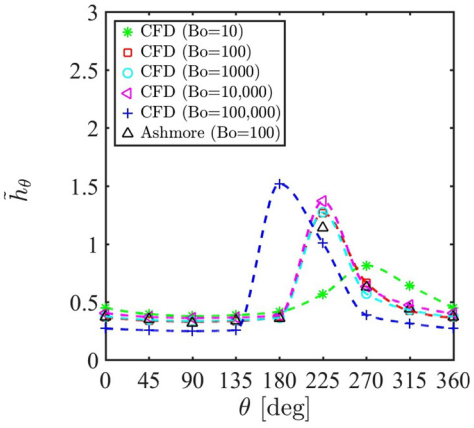

(b)

FIG. 14. (a) Contour plots of the volume fraction of liquid. From left to right: $Bo = 10$; $Bo = 100$; $Bo = 1000$; $Bo = 10\,000$; and $Bo = 100\,000$. (b) Calculated $\tilde{h}_\theta$ from the present CFD for $Bo = 10$–$100\,000$ together the solution from Ashmore *et al.* (2003) for $Bo = 100$. In all cases, $A = 0.1$, $\lambda = 3$, and $Re = 200$.

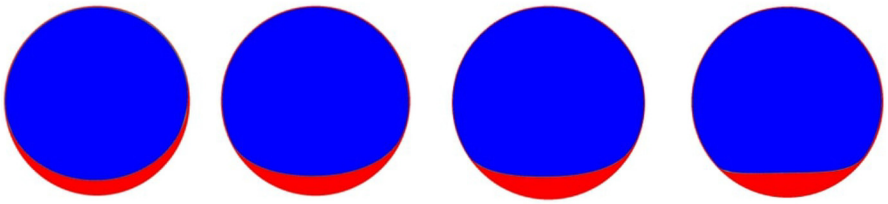

(a)

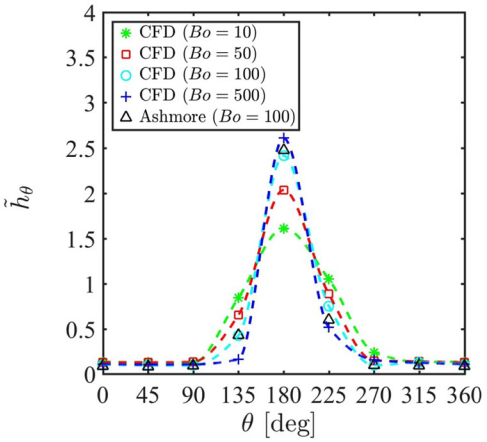

(b)

FIG. 15. (a) Contour plots of the volume fraction of liquid. From left to right: $Bo = 10$; $Bo = 50$; $Bo = 100$; and $Bo = 500$. (b) Calculated $\tilde{h}_\theta$ from the present CFD for $Bo = 10$–$100\,000$ together the solution from Ashmore *et al.* (2003) for $Bo = 100$. In all cases, $A = 0.1$, $\lambda = 50$, and $Re = 12$.

applications would contain air–oil mixtures at significantly higher Reynolds and Bond numbers. Thus, we performed simulations in a relatively large range of both *Re* and *Bo*, which falls outside the range for which we have validated our model.

First, we conducted simulations in a case with a small filling fraction *A*, and large *Re* and *Bo* as follows: $A = 0.02$; $Bo = 2.2 \times 10^5$; and $\lambda = 2, 5$, and 20, which correspond to $Re = 1.07 \times 10^5, 4.27 \times 10^4$, and 9.49×10^3, respectively. Figures 16(a) and 16(b), respectively, show contour plots of the volume fraction of liquid and simulated $\tilde{h}_\theta$ for $\lambda = 2, 5$, and 20. It can be observed that the rimming flow is in the shear-dominated regime for $\lambda = 2$, the transitional regime for $\lambda = 5$, and the gravitational-dominated regime for $\lambda = 20$. This shows that three flow regimes can be achieved at nearly the same range of λ suggested by the previous analytical model for lower *Re* and *Bo* when *A* is small enough. It is also found that the peak of $\tilde{h}_\theta$ for $\lambda = 20$ is significantly larger than the predicted analytical solution for the same λ (see, e.g., Fig. 11). For lower λ, however, there seems a closer match between the present solutions for low *A* and the analytical predictions by Ashmore *et al.* (2003). Overall, the above observation would suggest that the filling fraction could have a potential role in the appearance of the specific rimming flow regimes.

Then, we conducted simulations for a larger filling fraction of $A = 0.1$, while λ was varied from 2 to 400. In these simulations, the Reynolds number was varied from $Re = 2.56 \times 10^6$ to $Re = 1.26 \times 10^4$, whereas the Bond number was fixed at $Bo = 4.55 \times 10^4$. As shown in Fig. 17, it was found that the shear-dominated regime, with

(a)

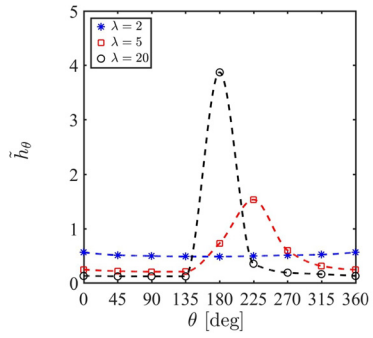

(b)

FIG. 16. (a) Contour plots of the volume fraction of liquid. From left to right: $\lambda = 2$ ($Re = 1.07 \times 10^5$); $\lambda = 5$ ($Re = 4.27 \times 10^4$); and $\lambda = 20$ ($Re = 9.49 \times 10^3$). (b) Calculated $\tilde{h}_\theta$ for $\lambda = 2 - 20$. In all cases, $A = 0.02$ and $Bo = 2.2 \times 10^5$.

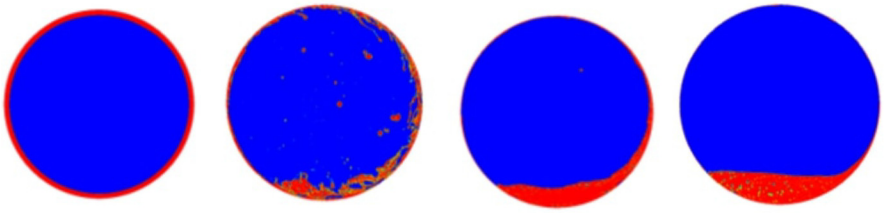

(a)

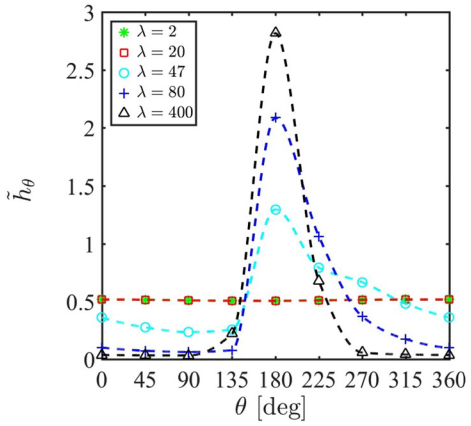

(b)

FIG. 17. (a) Contour plots of the volume fraction of liquid. From left to right: $\lambda = 20$ ($Re = 2.54 \times 10^5$); $\lambda = 47$ ($Re = 1.09 \times 10^5$); $\lambda = 80$ ($Re = 6.35 \times 10^4$); and $\lambda = 400$ ($Re = 1.26 \times 10^4$). (b) Calculated $\tilde{h}_\theta$ for $\lambda = 2 - 400$. In all cases, $A = 0.1$ and $Bo = 4.55 \times 10^4$.

a fully uniform distribution of liquid, was formed for $\lambda = 2$–20. The results only showed a transition from a shear-dominated regime at $\lambda = 47$. A pool regime instead appeared at very large $\lambda = 80$ with a significant raising of the film inside the cylinder. A gravitational number of $\lambda = 400$ was needed to observe a fully pooled flow. The plot for $\tilde{h}_\theta$ [Fig. 17(b)] clearly shows the increase in the peak of film thickness at $\theta = 180°$ with increasing λ. These results would clearly show that the traditional three flow regimes of the rimming flow are still attainable at nearly large A, Re, and Bo; however, they obviously fall within a different range of λ than the analytical predictions, which were valid for lower Re and Bo.

1. Effects of the Bond number

In this section, we studied the effects of the Bond number on the flow behavior for $Re > 1000$. Here, the Bond number has been varied through changing values of surface tension, with Bo varied between $Bo = 22.3$ and $Bo = 4.55 \times 10^4$. It should be noted that no significant changes were observed below or above this range of Bond numbers. Figure 18 shows plots of numerical simulations for the case with $A = 0.1$ and $\lambda = 47$. It was found that the rimming flow was moving toward a near-uniform shear-dominated regime with decreasing Bo. As can be seen in Fig. 18(b), the largest thickness of the liquid decreased as Bo decreased. Together with previously discussed results at lower Re, these observations would suggest that the rimming flow tends to transition from a shear-dominated flow regime to a pooling regime with increasing Bo.

C. A parameter space for the existence of different flow regimes

The previously discussed results show that three different flow regimes of shear-dominated (smooth), transitional (shock), and gravitational-dominated (pool) are attainable for a 2D rimming flow under a variety of different parameters, including the gravitational number (λ), Reynolds number (Re), Bond number (Bo), and filling fraction (A). The previous analytical solutions (Ashmore *et al.*, 2003) categorized three regimes only based on λ, assuming that Bo and Re are finite. Our additional CFD simulations performed beyond the imposed limitations of previous analytical investigations showed that the rimming flow regimes could be still achieved, albeit in different ranges of λ. In view of our finding that the effects of A, λ, Re, and Bo are crucial to form a rimming flow regime, we propose a combination of these numbers to identify all three regimes. As such, we defined two additional non-dimensionalized numbers, which are the Froude number defined as

$$Fr = \frac{\omega^2 R}{A^2 g} \tag{8}$$

and the capillary number defined as

$$Ca = \frac{\mu \omega R}{A^3 \sigma}. \tag{9}$$

It should be noted that in fact, the Froude number describes the ratio of Re/λ, whereas the capillary number indicates the ratio of Bo/λ. Figure 19 shows the newly introduced parametric space, which is based on combinations of A, Fr, and Ca for the existence of different flow regimes, namely, A^2Fr and A^2Ca. In this graph, both the present numerical data and previously reported analytical and experimental results are included. As can be seen, the data can clearly distinguish the shear-dominated regime mainly at large values of A^2Fr, whereas the pool regime is formed at smaller A^2Fr. The transitional regime lies

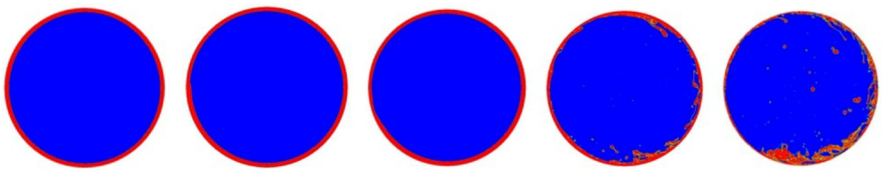

(a)

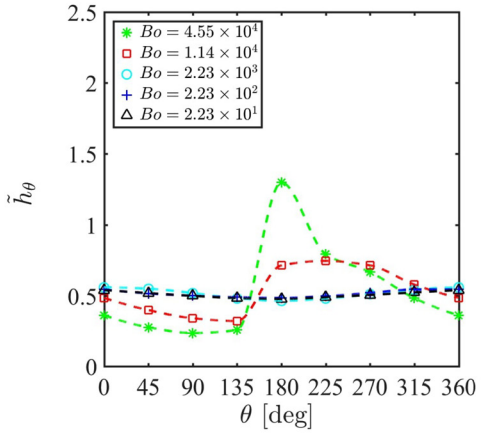

(b)

FIG. 18. (a) Contour plots of the volume fraction of liquid. From left to right: $Bo = 2.23$; $Bo = 2.23 \times 10^2$; $Bo = 2.23 \times 10^3$; $Bo = 1.14 \times 10^4$; and $Bo = 4.55 \times 10^4$ (b) Calculated $\tilde{h}_\theta$ for $\lambda = 2 - 400$. In all cases, $A = 0.1$, $\lambda = 47$, and $Re = 1.09 \times 10^5$.

between the two other regimes in a moderate-range of A^2Fr. At very large or small A^2Fr, no significant effects of the capillary number on the flow regimes can be found. However, it can be seen that for $0.1 \lesssim A^2Fr \lesssim 10$, increasing A^2Ca leads to rimming flow switching from a shear-dominated flow to transient or pool flows. It should be noted the dashed lines are proposed in Fig. 19 to tentatively distinguish regimes based on the current data.

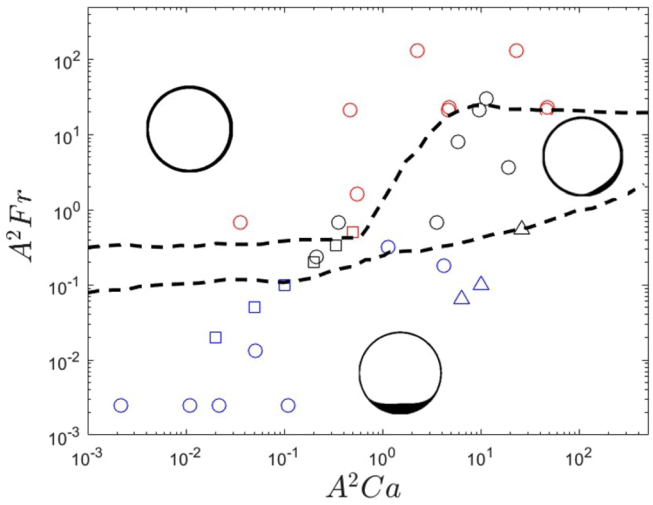

FIG. 19. Parameter space for the existence of different flow regimes. Red symbols highlight the shear-dominated regime, black symbols associate with the transition regime, and blue symbols identify the pool regime. Present CFD (◯); (Ashmore *et al.*, 2003) (□); (Tirumkudulu and Acrivos, 2001) (△). The dashed lines highlight boundaries between three regimes.

IV. CONCLUSIONS

This article describes the first CFD simulations of rimming flow in a partially filled horizontally rotating cylinder. We particularly studied three different regimes of thin-film flow, namely, shear-dominated, transient, and gravitational-dominated flows, for a broad range of parameter space. Aside from the intrinsic scientific interest, these phenomena deserve attention because of their presence in many industrial systems, notably aero-engine bearing chambers. The major objective of this work was to present a validated CFD model that is capable of identifying rimming flow regimes under different flow conditions, beyond what has been observed in the previous analytical and experimental investigations. Our adopted CFD method was successful in predicting the rimming flow regimes and resolving the interface between regions containing gas and liquid. We presented the results based on the Reynolds numbers and studied the effects of Bond numbers.

First, we simulated the rimming flow in low-to-medium Reynolds numbers: $Re \lesssim 1000$ and validated the present procedure against analytical and experimental results. We began by using low and finite Bond numbers to validate our work, then we separately studied the effects of Bond numbers. The flow regimes were identified through numerical solutions for volume fraction and thin-film thickness for different and vast combinations of gravitational number, Reynolds number, Bond number, and filling fraction. The CFD results nicely predicted that all three regimes were found to be in very good agreement with experimental and analytical values under comparable conditions.

In the next step, we investigated the rimming flow regimes in larger ranges of Reynolds and Bond numbers. While, for this larger range of parameters, no experimental data were available for validation; the shear-dominated, transient, and gravitational-dominated flows were still identified by the present CFD method, albeit under a different range of parameters. Future experimental work is recommended to study the flow regimes in larger ranges of Reynolds and Bond numbers.

Finally, we proposed a new map of rimming flow regimes, covering a broad range of parameter space. In this map, the shear-dominated, transient, and gravitational-dominated regimes existed and separated with the use of two additional parameters, namely, capillary number and Froude number, combined with the filling fraction.

ACKNOWLEDGMENTS

Financial support was provided by the MITACS and Pratt and Whitney Canada.

AUTHOR DECLARATIONS

Conflict of Interest

The authors have no conflicts to disclose.

DATA AVAILABILITY

The data that support the findings of this study are available from the corresponding author upon reasonable request.

REFERENCES

ANSYS, Ansys Fluent V20R2 User Guide, 2020.
Ashmore, J., Hosoi, A. E., and Stone, H. A., "The effect of surface tension on rimming flows in a partially filled rotating cylinder," J. Fluid Mech. **479**, 65–98 (2003).
Benilov, E. S., Benilov, M. S., and Kopteva, N., "Steady rimming flows with surface tension," J. Fluid Mech. **597**, 91–118 (2008).
Brackbill, J. U., Kothe, D. B., and Zemach, C., "A continuum method for modelling surface tension," J. Comput. Phys. **100**, 335–354 (1992).
Chen, P. J., Tsai, Y. T., Liua, T. J., and Wu, P. Y., "Low volume fraction rimming flow in a rotating horizontal cylinder," Phys. Fluids **19**, 128107 (2007).
Evans, P. L., Schwartz, L. W., and Roy, R. V., "Three-dimensional solutions for coating flow on a rotating horizontal cylinder: Theory and experiment," Phys. Fluids **17**, 072102 (2005).
Hernandez-Perez, V., Abdulkadir, M., and Azzopardi, B., "Grid generation issues in the CFD modelling of two-phase flow in a pipe," J. Comput. Multiphase Flows **3**, 13–26 (2011).
Hirt, C. W., and Nichols, B. D., "Volume of fluid (VOF) method for the dynamics of free boundaries," J. Comput. Phys. **39**, 201–225 (1981).
Johnson, R. E., "Steady-state coating flows inside a rotating horizontal cylinder," J. Fluid Mech. **190**, 321–342 (1988).
Kakimpa, B., Morvan, H., and Hibberd, S., "The depth-averaged numerical simulation of laminar thin-film flows with capillary waves," J. Eng. Gas Turbines Power **138**, 112501 (2016).
Kay, E. D., Hibberd, S., and Power, H., "Inertial effects at moderate Reynolds number in thin-film rimming flows driven by surface shear," Phys. Fluids **25**, 102108 (2013).
Kay, E. D., Hibberd, S., and Power, H., "A depth-averaged model for non-isothermal thin-film rimming flow," Int. J. Heat Mass Transfer **70**, 1003–1015 (2014).
Kumawat, T. C., and Tiwari, N., "Stability analysis of rimming flow inside a horizontally rotating cylinder in the presence of an insoluble surfactant," Phys. Fluids **29**, 122102 (2017a).
Kumawat, T. C., and Tiwari, N., "Stability analysis of the rimming flow inside a uniformly heated rotating horizontal cylinder," Phys. Fluids **29**, 032102 (2017b).
Kumawat, T. C., and Tiwari, N., "Hydrodynamic stability of thermoviscous liquid film inside a rotating horizontal cylinder: Heating and cooling effects," Phys. Fluids **30**, 032103 (2018).
Mecke, K., and Rauscher, M., "On thermal fluctuations in thin film flow," J. Phys.: Condens. Matter **17**, 3515–3522 (2005).
Menter, F. R., Kuntz, M., and Langtry, R., "Ten years of experience with the SST turbulence model," in *Turbulence, Heat and Mass Transfer*, edited by K. Hanjalic, Y. Nagano, and M. Tummers (Begell House, Inc., 2003), pp. 625–632.
Mitchell, A. J., Duffy, B. R., and Wilson, S. K., "Unsteady coating flow on a rotating cylinder in the presence of an irrotational airflow with circulation," Phys. Fluids **34**, 043105 (2022).
Moffatt, H. K., "Behaviour of a viscous film on the outer surface of a rotating cylinder," J. Mec. **16**, 651–673 (1977).
Nicholson, J. M. P., Power, H., Tammisol, O., Hibberd, S., and Kay, E. D., "Fluid dynamics of the slip boundary condition for isothermal rimming flow with moderate inertial effect," Phys. Fluids **31**, 033602 (2019).
O'Brian, S. B. G., and Gath, E. G., "The location of a shock in a rimming flow," Phys. Fluids **10**, 10401042 (1988).
O'Brian, S. B. G., and Schwartz, L. W., "Theory and modeling of thin film flows," Encycl. Surf. Colloid Sci. **4**, 5283–5297 (2002).
Ruschak, K. J., and Scriven, L. E., "Rimming flow of liquid in a rotating cylinder," J. Fluid Mech. **76**, 113–126 (1976).
Singaram, S. S., Lodha, H., and Jachuck, R. J., "Experimental investigation of continuous single-phase rimming flow in a horizontal rotating cylinder," AIChE J. **60**, 3939–3950 (2014).
Singh, P., Venkatesan, R., Fogler, H. S., and Nagarajan, N., "Formation and aging of incipient thin film wax-oil gels," AIChE J. **46**, 1059–1074 (2004).
Thoroddsen, S. T., and Mahadevan, L., "Experimental study of instabilities in a partially-filled horizontally-rotating cylinder," Exp. Fluids **23**, 1–13 (1997).
Tirumkudulu, M., and Acrivos, A., "Coating flows within a rotating horizontal cylinder: Lubrication analysis, numerical computations, and experimental measurements," Phys. Fluids **13**, 14–19 (2001).
Willems, G. P., Kroes, J. P., Golombok, M., van Esch, B. P. M., van Kemenade, H. P., and Brouwers, J. J. H., "Performance of a novel rotating gas-liquid separator," J. Fluids Eng. **132**, 031301 (2010).